Correspondence to:
L. M. Bjoland,
lindis.m.bjoland@uit.no

Interplanetary magnetic field and solar cycle dependence of Northern Hemisphere *F* region joule heating

L. M. Bjoland[1], X. Chen[2,3,4], Y. Jin[3], A. S. Reimer[5], Å. Skjæveland[2,3], M. R. Wessel[5], J. K. Burchill[6], L. B. N. Clausen[3], S. E. Haaland[4,7], and K. A. McWilliams[5]

[1]Department of Physics and Technology, University of Tromsø-The Arctic University of Norway, Tromsø, Norway, [2]Department of Arctic Geophysics, University Centre in Svalbard, Longyearbyen, Norway, [3]Department of Physics, University of Oslo, Oslo, Norway, [4]Birkeland Centre for Space Science, University of Bergen, Bergen, Norway, [5]Institute of Space and Atmospheric Studies, University of Saskatchewan, Saskatoon, Saskatchewan, Canada, [6]Department of Physics and Astronomy, University of Calgary, Calgary, Alberta, Canada, [7]Max-Planck Institute for Solar Systems Research, Göttingen, Germany

Abstract Joule heating in the ionosphere takes place through collisions between ions and neutrals. Statistical maps of *F* region Joule heating in the Northern Hemisphere polar ionosphere are derived from satellite measurements of thermospheric wind and radar measurements of ionospheric ion convection. Persistent mesoscale heating is observed near postnoon and postmidnight magnetic local time and centered around 70° magnetic latitude in regions of strong relative ion and neutral drift. The magnitude of the Joule heating is found to be largest during solar maximum and for a southeast oriented interplanetary magnetic field. These conditions are consistent with stronger ion convection producing a larger relative flow between ions and neutrals. The global-scale Joule heating maps quantify persistent (in location) regions of heating that may be used to provide a broader context compared to small-scale studies of the coupling between the thermosphere and ionosphere.

1. Introduction

Energy from the solar wind drives magnetospheric and ionospheric plasma convection mostly through reconnection of the interplanetary magnetic field (IMF) and the geomagnetic field [*Dungey*, 1961; *Cowley*, 2000]. At high latitudes, in the *F* region (above 150 km altitude) ions follow a global-scale $\mathbf{E} \times \mathbf{B}$ circulation pattern typically characterized by antisunward flow over the poles and sunward return flow at lower latitudes [e.g., *Cowley and Lockwood*, 1992]. Field-aligned currents (FACs) are also important in magnetosphere-ionosphere coupling; however, FACs primarily close as Pedersen currents in the *E* region of the ionosphere (below 150 km altitude), where the Pedersen conductivity is larger and FACs can dissipate energy via Joule heating [e.g., *Wilder et al.*, 2012]. The present study focuses on discussing the energy dissipated in the *F* region through collisions between ions and neutrals.

Thermospheric neutral circulation is driven by pressure gradients (due to solar heating, Joule heating, and particle precipitation) and ion drag from ionospheric plasma circulation [e.g., *Fuller-Rowell and Rees*, 1980; *Hays et al.*, 1979]. A notable equatorward deflection of the thermospheric wind in the dusk sector is caused by the combination of the Coriolis and centrifugal forces. In contrast, a less significant deflection is found in the dawn sector where the two forces tend to cancel [*Gundlach et al.*, 1988].

Most energy coupling between neutrals and ions takes place through collisions, resulting in frictional heating and momentum transfer [e.g., *Hays et al.*, 1973]. *St.-Maurice and Hanson* [1982] used the ion energy equation to calculate Joule heating in the *F* region. They found that the ion-neutral temperature difference due to Joule heating can be estimated from the relative flow:

$$m_n \left(\mathbf{V}_i - \mathbf{V}_n \right)^2 \approx 3 k_B \left(T_i - T_n \right), \tag{1}$$

where $\mathbf{V}_i$ and $\mathbf{V}_n$ are the ion and neutral velocities, respectively; T_i and T_n are the ion and neutral temperatures; m_n is the average mass of one neutral particle; and k_B is Boltzmann's constant. Due to several assumptions made by *St.-Maurice and Hanson* [1982], equation (1) is valid in the high-latitude *F* region between altitudes of 250 km and 500 km. In summary, the assumptions include the following: measurement time scales in excess of $1/v_{in}$ (where v_{in} is the ion-neutral collision frequency), incompressible ion velocity,

weak viscous heating on large spatial scales, negligible heat conduction and heat advection, and no relative ion-electron drift. These assumptions allow several of the terms in the ion energy equation to be discarded.

Previous experimental studies of Joule heating have focused on small-scale measurements. For example, *St.-Maurice and Hanson* [1982] studied satellite measurements of ion temperature and used those to calculate neutral temperature. They observed Joule heating in the postnoon and postmidnight sectors but focused on data from only a few orbits. *Baron and Wand* [1983] used the Chatanika and Millstone Hill incoherent scatter radars (ISRs) to measure ion temperature in two experiments during the summer of 1981. They observed significantly greater Joule heating enhancement of ion temperature in the morning sector than in the evening sector and attributed this to differences between the neutral wind in the morning and evening sectors. *Davies et al.* [1997] used ISR to measure ion temperature at a fixed geographic latitude for many local times. They observed the greatest rate of occurrence of Joule heating in the postmidnight sector. Recently, *Goodwin et al.* [2014] observed F region ion temperature "spikes" using the Poker Flat ISR located at 60° magnetic latitude (MLAT). These spikes were attributed to an expansion of the convection pattern that caused an increased ion-neutral relative drift, resulting in enhanced Joule heating on the expanding boundary of the convection pattern.

Numerical models of localized heating are widely used in case studies. For example, *Cooper et al.* [2009] included Joule heating in a local-scale model of vertical thermospheric winds. *Davies et al.* [1995] compared ISR measurements with results from the Sheffield University Plasmasphere and Ionosphere Model, calculating parameters along a single magnetic field line. *Heelis and Coley* [1988] used a model to produce maps of Pedersen conductivity and Joule heating from satellite measurements of ion velocity.

Global-scale maps of F region Joule heating in high-latitude regions have been simulated using numerical models [e.g., *Deng and Ridley*, 2007; *Zhang et al.*, 2011] and have predicted two- and three-cell patterns. The magnitude of Joule heating predicted by global models is often less than that calculated with local models. This is typically explained as being due to poor resolution of small-scale heating features by the large-scale models [*Deng and Ridley*, 2007].

In contrast to small-scale measurements, global maps may help resolve spatiotemporal ambiguities for individual small-scale measurements (e.g., measurements from satellites or ISRs). The aim of the present study is to demonstrate that the technique of *St.-Maurice and Hanson* [1982] can be used to produce global-scale maps of F region Joule heating by combining satellite measurements of neutral wind with radar measurements of ion velocity.

2. Data and Methodology

In this study we combine F region ion convection velocity data and F region neutral wind data using equation (1) to produce global-scale maps of F region Joule heating. Ion velocity vectors were obtained from the Super Dual Auroral Radar Network (SuperDARN) of high-frequency (HF) over-the-horizon radars [*Greenwald et al.*, 1995], having been derived using the statistical model of *Ruohoniemi and Baker* [1998]. In general, SuperDARN may be used to study a broad range of ionospheric and magnetospheric phenomena, including the structure and dynamics of ionospheric convection, flux transfer events, and field-aligned currents [*Chisham et al.*, 2007]. Global maps of ionospheric convection are often used to provide essential complementary information on a global scale for smaller-scale measurements [e.g., *Zhang et al.*, 2013].

Neutral wind data were obtained from the CHAMP satellite that was launched in July 2000. CHAMP orbited the Earth at an inclination of 87.3° with an initial altitude of 456 km [*Reigber et al.*, 2002] that decayed to 250 km before reentry of the satellite in late 2010. Only CHAMP neutral wind measurements from an altitude above 250 km were used in this study, in accordance with the applicability limits of equation (1). CHAMP carried a triaxial accelerometer designed to measure orbital perturbations caused by the interaction of the satellite with the atmosphere of the Earth [*Reigber et al.*, 2002]. The cross-track neutral wind data have been derived from the accelerometer data using an iterative method described in *Doornbos et al.* [2010]. In that method, atmospheric velocity relative to the spacecraft is combined with observed and modeled aerodynamic accelerations to calculate the cross-track wind. An estimate of the cross-track neutral wind measurement error was also used in this study, accounting for the precision of the accelerometer (20 m/s) and for systematic errors (15 m/s) [*Liu et al.*, 2006]. An additional error of 10% of the measured cross-track
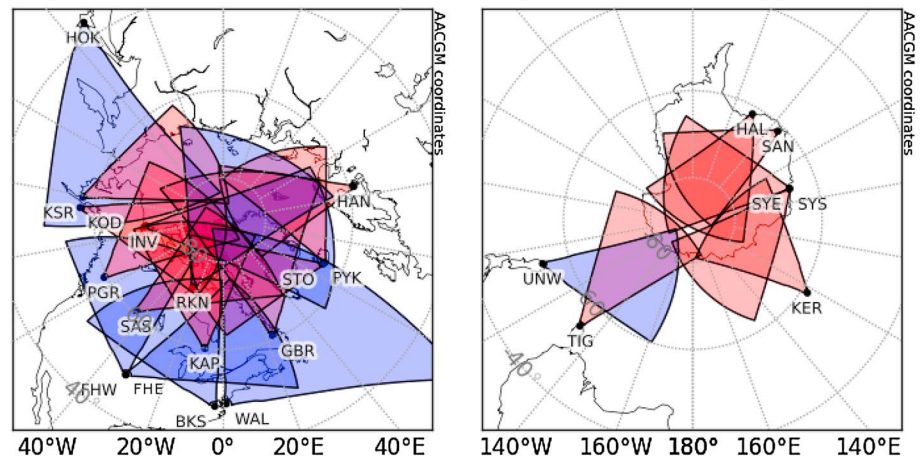
Figure 1. SuperDARN in the Northern (left) and Southern (right) Hemispheres, 2001–2009. Radar site locations are marked with black dots and identifying letter codes and the fan-shaped fields of view are colored in. Red fields of view indicate radars that were operational for approximately the entire period and blue fields of view indicate radars that began operations during or shortly before the solar minimum portion of the period (2005–2009).

wind was also included to account for uncertainty introduced by neglecting any contribution from the along-track wind, which can be significant in polar regions [*Förster et al.*, 2008].

Data for the years 2001 to 2009 from SuperDARN and CHAMP were gridded spatially and categorized by IMF orientation and solar cycle. Only SuperDARN data that were spatially and temporally coincident with CHAMP measurements were used. The Altitude Adjusted Corrected Geomagnetic (AACGM) coordinate system [*Baker and Wing*, 1989] is used in this paper. Equal-area cells in MLAT and magnetic local time (MLT) were used. Each cell is approximately 200 km × 400 km in size (2° × 4° at the equator). IMF data in geocentric solar magnetospheric (GSM) coordinates from the OMNI data set [*King and Papitashvili*, 2005] were used to partition the SuperDARN and CHAMP data into eight IMF clock angle ranges, where the clock angle θ_{IMF} is defined as

$$\theta_{IMF} = \arctan\left(\frac{B_y}{B_z}\right), \tag{2}$$

where B_y and B_z are the GSM y and z components of the IMF, respectively. The ranges have equal angular sizes and each one is centered on an axis or a 45° line; for example, the $+B_z$ range extends 22.5° in either direction from the $+B_z$ axis, the $+B_y$ range extends 22.5° in either direction from the $+B_y$ axis, and the $+B_z/+B_y$ range is between those two, centered on the $B_z = B_y$ line. Two solar cycle categories were used: one for solar maximum years (2001–2004) and one for solar minimum years (2005–2009).

Only measurements of cross-track neutral winds were available from CHAMP. In order to produce statistical maps of the thermospheric neutral wind vector field, the forward model was solved to obtain two-dimensional (2-D) wind vectors. The model is written

$$\vec{v}_c = \mathbf{A}\vec{v} + \vec{e}, \tag{3}$$

where $\vec{v}_c$ is a column vector of the magnitudes of the cross-track wind measurements in the direction of the horizontal unit vectors stored in the rows of matrix $\mathbf{A}$, $\vec{v}$ is the velocity vector being sampled by CHAMP, and $\vec{e}$ is a vector of the cross-track wind measurement error estimates. Solving equation (3) for $\vec{v}$ yields 2-D neutral wind vectors.

The weighted least squares (WLS) method described in *Strutz* [2010] and the Bayesian method described in *Heinselman and Nicolls* [2008] were both employed to invert equation (3) to obtain $\vec{v}$. Each statistical method was used to yield an average 2-D wind vector from all the cross-track measurements for each spatial grid point. The WLS method is similar to the method used by *Förster et al.* [2008], the difference being that the WLS method includes an error estimate weighting of the cross-track wind measurements. As in *Förster et al.* [2008], singular value decomposition was used to calculate the Moore–Penrose pseudoinverse of matrix $\mathbf{A}$.

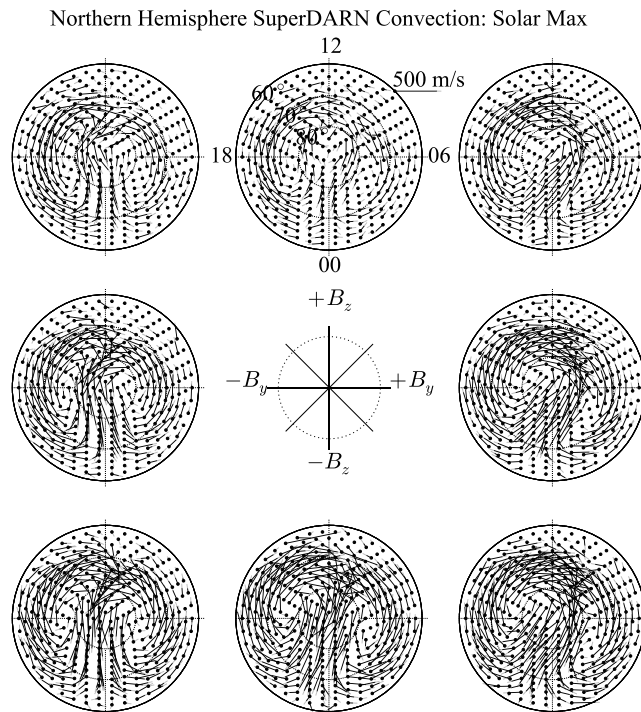Northern Hemisphere SuperDARN Convection: Solar Max

Figure 2. Northern Hemisphere SuperDARN ion convection categorized by IMF orientation during solar maximum (2001–2004). Each panel shows ion velocity from 60° to the pole in AACGM MLAT and MLT coordinates with magnetic noon at the top. Barb length indicates velocity magnitude with the base of the vector indicated by a dot. There is one panel for each of the eight IMF clock angle categories as indicated by the compass at the center of the figure.
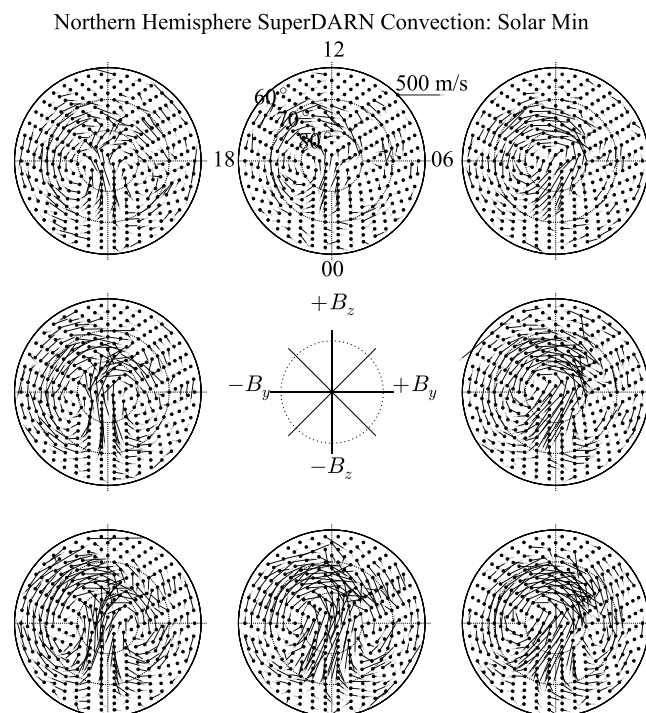
Northern Hemisphere SuperDARN Convection: Solar Min

Figure 3. Same as Figure 2 but for solar minimum (2005–2009).

The WLS method and the Bayesian method resulted in comparable solutions, with the largest differences between corresponding vectors being less than 1%, so we are confident in the results.

Only Northern Hemisphere data are presented in this study. SuperDARN coverage in the Southern Hemisphere for the 2001–2009 period was generally poorer than in the Northern Hemisphere (see Figure 1). This, combined with the strict selection criteria imposed on the SuperDARN data set, reduced the Southern Hemisphere statistics to an inadequate level. Only CHAMP measurements that occurred above 250 km altitude were utilized (in accordance with the assumptions required for equation (1)). Similarly, only F region SuperDARN measurements were used in this study [see *Ruohoniemi and Baker*, 1998].

Figures 2 and 3 show statistical F region ion velocity maps for solar maximum and solar minimum periods, respectively. Each vector indicates the mean of all fitted SuperDARN velocity vectors in a spatial grid cell that occurred within 4 min of any CHAMP measurement in the same spatial cell. The fitted velocities were obtained from 2 min resolution ion convection maps that had been produced using the method of *Ruohoniemi and Baker* [1998]. Only fitted velocities from convection map cells that contained SuperDARN line-of-sight measurements were used. When produced from measurements, the fitted velocities are well constrained by and in agreement with observations [*Ruohoniemi and Baker*, 1998]. For Figure 2, above 80° MLAT the mean number of SuperDARN data points per grid cell was 4112, between 70° and 80° MLAT it was 3300, and below 70° MLAT it was 526. For Figure 3, above 80° MLAT the mean number of SuperDARN data points per grid cell was 3352, between 70° and 80° MLAT it was 1761, and below 70° MLAT it was 307.

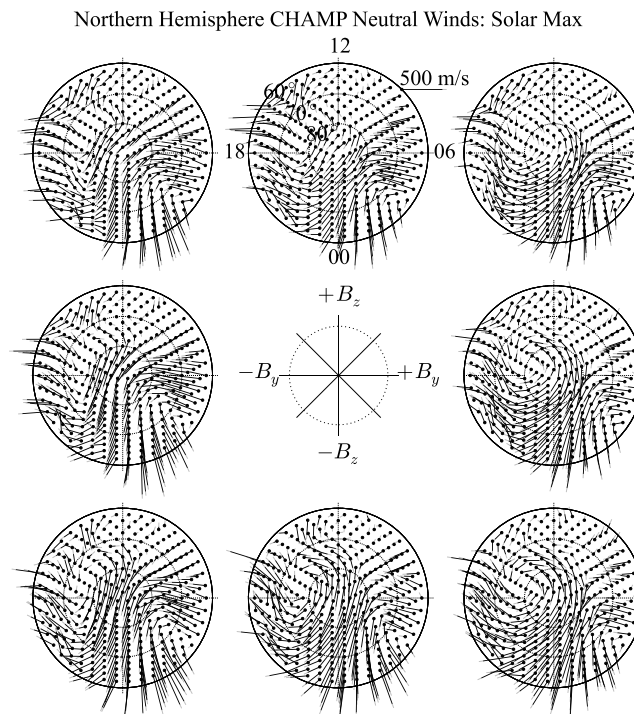The IMF and solar cycle dependence of the ion convection patterns in

Figure 4. CHAMP thermospheric winds in the Northern Hemisphere during solar maximum (2001–2004) organized in the same format as Figure 2.

between 70° and 80° MLAT it was 1013, and below 70° MLAT it was 508. For Figure 5, above 80° MLAT the mean number of data per grid cell was 1850, between 70° and 80° MLAT it was 807, and below 70° MLAT it was 404.
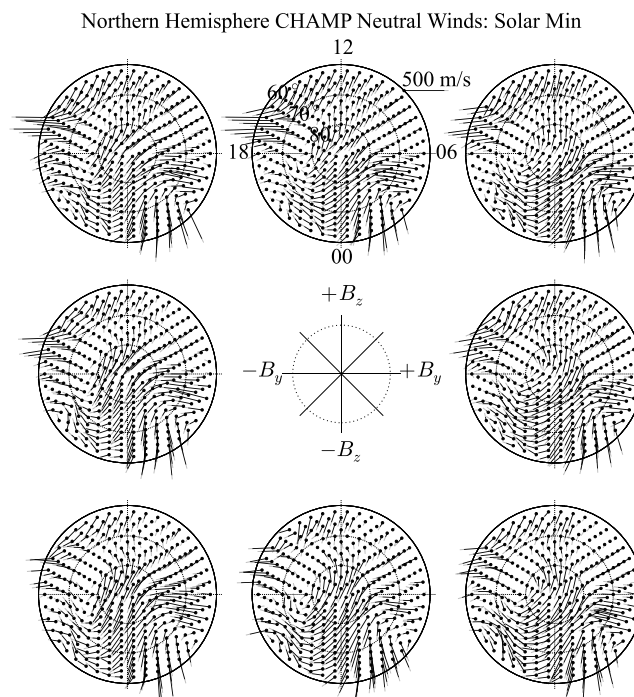
Figures 2 and 3 are consistent with what is typically observed [e.g., *Ruohoniemi and Baker*, 1998; *Ruohoniemi and Greenwald*, 2005; *Cousins and Shepherd*, 2010]. Specifically, a typical two-cell ion convection pattern that depends on IMF clock angle is observed. The largest ion velocities are observed for IMF $+B_y$ and $-B_z$ conditions. The ion convection patterns show a dawn-dusk asymmetry between cells of the convection pattern. The asymmetry varies with IMF B_y conditions; specifically, there is an elongation of the dawn (dusk) sector cell and rounding of the dusk (dawn) sector cell under IMF $+B_y$ (IMF $-B_y$) conditions.

Figures 4 and 5 show the 2-D neutral wind velocity vectors resulting from the WLS method. The figures show average F region thermospheric winds for the Northern Hemisphere categorized by IMF clock angle during solar maximum years (2001–2004) and solar minimum years (2005–2009), respectively. For Figure 4, above 80° MLAT the mean number of data per grid cell was 2323,

Figure 5. Same as Figure 4 except during solar minimum (2005–2009).

The neutral winds shown in Figures 4 and 5 are generally consistent with the maps of thermospheric winds presented in *Förster et al.* [2008]. For example, in the dusk sector, the persistent clockwise vorticity in the neutral wind pattern that we observe (near 80° MLAT and 17 MLT) was also reported by *Förster et al.* [2008]. The vorticity is more pronounced and the pattern becomes more circular in shape for the solar maximum period and for $+B_y$ and $-B_z$ IMF conditions. This is similar to the behavior observed in the ion velocity where a more circular pattern with stronger vorticity is also observed near 80° MLAT and 17 MLT for the solar maximum period and $+B_y$ and $-B_z$ IMF conditions. The clockwise vorticity in the neutral winds is driven by the combination of the Coriolis and centrifugal forces [*Gundlach et al.*, 1988] and seems to be supported or enhanced through interaction with ion convection. In contrast, there is counterclockwise
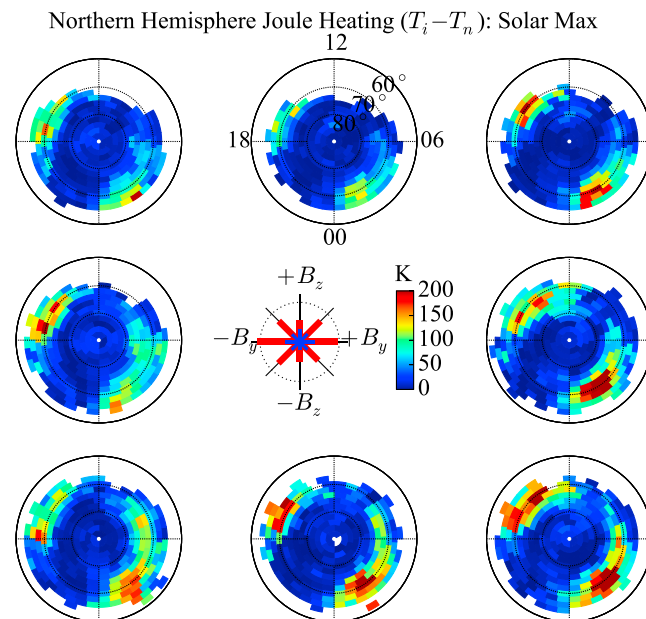
Northern Hemisphere Joule Heating ($T_i - T_n$): Solar Max

Figure 6. *F* region Joule heating in the Northern Hemisphere during solar maximum (2001–2004), plotted in a format similar to that of Figure 2. The temperature difference $T_i - T_n$ is indicated by the color of each grid cell. The red and blue lines in the compass represent the number of measurements from SuperDARN and CHAMP, respectively, used in each map. The radius of the dashed circle on the compass represents 10^6 measurements.

vorticity observed in the dawnside neutral wind pattern near 70° MLAT and 3 MLT that does not appear to vary greatly with IMF orientation or solar cycle.

A stagnation in the neutral wind (see Figures 4 and 5) is observed during solar maximum between 65° and 75° MLAT and from 8–12 MLT, but it is not observed during solar minimum. During solar maximum, increased ionospheric density increases the number of collisions between ions and neutrals and increased ionospheric flow yields more momentum transfer per collision, as specified by the ion energy equation [e.g., *St.-Maurice and Hanson*, 1982, equation (1)]. On average, a larger number of collisions between ions and neutrals would produce the observed stagnation in the neutral winds. We note that *Förster et al.* [2008] also observed a stagnation of the neutral winds in the cusp region.

While the neutral wind is largely driven by solar heating [*Gundlach et al.*, 1988], Figures 4 and 5 do show a weak dependence on IMF orientation. Because the ion convection velocity depends on IMF conditions and because neutral wind flows can be modified by ions through collisions [*St.-Maurice and Hanson*, 1982], it is likely that the weak dependence of neutral wind on IMF orientation is due to the influence of the motion of the ions through ion-neutral collisions.
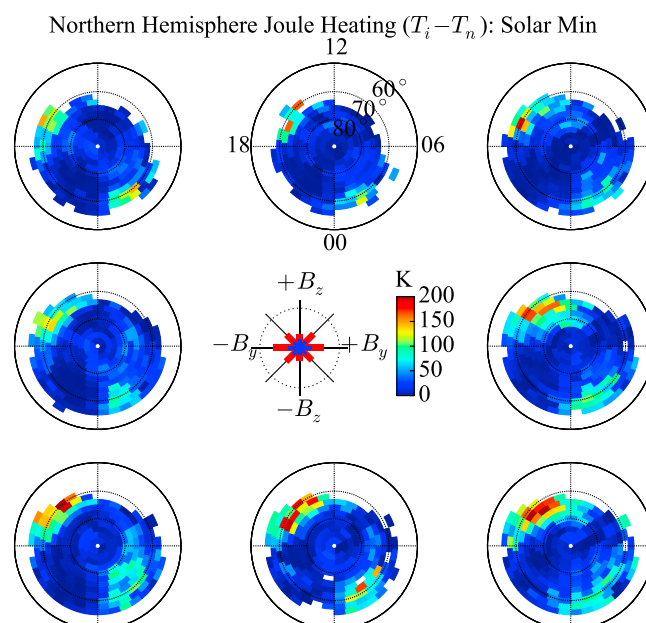
Northern Hemisphere Joule Heating ($T_i - T_n$): Solar Min

Figure 7. Same as Figure 6 except for solar minimum (2005–2009).

Maps of *F* region Joule heating were produced by combining the derived 2-D neutral wind velocity vectors and the SuperDARN ion velocity vectors using equation (1). Specifically, the temperature difference between ions and neutrals ($T_i - T_n$) was calculated. To ensure statistical significance, any average ion velocity vector derived from fewer than 500 measurements was discarded (i.e., with statistical error <5%). The maps of Joule heating were organized in the same way as the CHAMP and SuperDARN data using the same grid cells and categorization by IMF clock angle and the portion of the solar cycle.

The value of m_n for equation (1) appears as a scaling factor and was approximated as the mass of atomic oxygen, an assumption verified by the NRLMSISE-00 model for the altitude range covered by this study (250 km to 450 km) [*Picone et al.*, 2002]. We also assumed that for our

Table 1. Summary of Joule Heating Results for Solar Maximum[a]

IMF Orientation	Maximum Heating (K)	Grid Cells Out of 359 With:	
		Heating ≥100 K	Useable Data
$+B_z$	188	12	184
$+B_z/+B_y$	279	43	201
$+B_y$	400	72	233
$-B_z/+B_y$	447	88	229
$-B_z$	429	81	220
$-B_z/-B_y$	391	75	233
$-B_y$	344	47	218
$+B_z/-B_y$	251	25	197

[a]As shown in Figure 6. Note that the maximum heating values in this table correspond to the postmidnight heating region because it is the dominant heating region during solar maximum. The total of 359 grid cells includes all those above 60° MLAT.

purposes, neither the neutral wind nor the ion velocity varies with altitude over that range. *Deng and Ridley* [2007] found $|\mathbf{V}_i - \mathbf{V}_n|$ to be nearly constant in the altitude range covered by the present study.

3. Results and Discussion

Figures 6 and 7 show color maps of Joule heating produced by combining SuperDARN ion convection velocities (Figures 2 and 3) and CHAMP-derived neutral wind velocities (Figures 4 and 5) using equation (1). The white grid cells indicate regions that have fewer than 500 measurements available and thus are excluded to ensure statistical significance.

In contrast to previous case studies of localized Joule heating, the current study finds statistically significant persistent regions of Joule heating in the high-latitude *F* region. A distinct dawn-dusk asymmetry in Joule heating—specifically two persistent regions of Joule heating located in the postnoon and postmidnight MLT regions—is observed for all IMF orientations and for both solar maximum and solar minimum periods. The postnoon region is generally centered at about 70° MLAT and 15 MLT and the postmidnight region is generally centered at about 70° MLAT and 2 MLT.

Comparing the Joule heating plots with the neutral wind plots, one can see that the postnoon heating region is colocated with eastward zonal neutral winds and the postmidnight heating region is colocated with westward zonal neutral winds. From equation (1), one would expect to observe the ion velocity in these two regions to have a strong antiparallel component compared to the neutral wind velocity. Indeed, examination of the ion velocity plots in Figures 2 and 3 confirms these expectations.

The magnitude and extent of the regions of Joule heating are observed to vary with both IMF orientation and solar cycle. During solar maximum, the postmidnight region generally has a larger magnitude of Joule heating than the postnoon region. The magnitude of heating is observed to be larger under $-B_z$ and $+B_y$ IMF conditions than it is under $+B_z$ and $-B_y$ conditions. Also, under IMF $-B_z$ conditions, the more negative the IMF B_y, the larger the observed zonal extent of the postmidnight heating region toward the prenoon sector. During solar minimum Joule heating in the postmidnight region is less pronounced; instead, the postnoon heating region dominates. The magnitude of the Joule heating is generally lower for solar minimum than for solar maximum. Tables 1 and 2 quantitatively summarize the heating results.

Table 2. Summary of Joule Heating Results for Solar Minimum[a]

IMF Orientation	Maximum Heating (K)	Grid Cells Out of 359 With:	
		Heating ≥100 K	Useable Data
$+B_z$	150	2	152
$+B_z/+B_y$	159	16	186
$+B_y$	241	31	207
$-B_z/+B_y$	298	45	210
$-B_z$	251	47	196
$-B_z/-B_y$	227	29	212
$-B_y$	181	16	210
$+B_z/-B_y$	182	12	170

[a]As shown in Figure 7. Note that the maximum heating values in this table correspond to the postnoon heating region because it is the dominant heating region during solar minimum. The total of 359 grid cells includes all those above 60° MLAT.

Our results are complementary to previous studies of Poynting flux energy input. For example, whereas we obtain persistent regions of heating (in the *F* region) centered around 2 MLT and 15 MLT regardless of IMF orientation, *Knipp et al.* [2011] found a pattern of large Poynting flux into the ionosphere for large IMF B_y conditions centered around 10–12 MLT and 70° MLAT. *Wilder et al.* [2012] found increased Joule heating rates due to FACs associated with fast ionospheric flow channels near the ionospheric footprint of the magnetospheric cusp under strong IMF B_y conditions, whereas we did not observe strong heating associated with the cusp. It is apparent that combining the techniques used in studies like [*Knipp*

et al., 2011] and *Wilder et al.* [2012] with the technique used in the present study can yield a more complete understanding of the dissipation of magnetospheric energy in the ionosphere.

A statistical study by *Davies et al.* [1997], using 4000 hours of ISR data from observations between October 1984 and December 1995, found that the occurrence rate of Joule heating peaked during the night with a preference for the postmidnight sector at 67° MLAT, which is consistent with the results obtained in our study. *Davies et al.* [1997] also found that the magnitude of the heating was between 120 K and 500 K, whereas we find the magnitude of heating to be ∼350 K on average.

St.-Maurice and Hanson [1982] observed local (small-scale) Joule heating in the postnoon and postmidnight sectors near 70° magnetic latitude. This is consistent with the heating regions observed in Figures 6 and 7. *St.-Maurice and Hanson* [1982] measured significantly larger values of Joule heating (∼1500 K); however, their study excluded heating events below 200 K and only contained highly localized measurements (with a finer spatial resolution than our grid).

Differences in the magnitude of Joule heating in the results of *St.-Maurice and Hanson* [1982] and *Davies et al.* [1997] and of the present study are likely due to differences in spatial and temporal averaging between data sets. For example, high-resolution in situ satellite measurements were used in *St.-Maurice and Hanson* [1982] and the ISR measurements of *Davies et al.* [1997] were made on time scales of the order of minutes with spatial scales less than 1000 km^2. In contrast, the Joule heating in each grid cell in the maps presented in Figures 6 and 7 is an average over approximately 80,000 km^2 of space and over 4 years, meaning the contributions of any large-amplitude or short-lived heating events that occurred are weakened.

In contrast to *Deng and Ridley* [2007], a study of the importance of electric field variability in accounting for all heating, the current study focuses on quantifying the steady or "DC" component of Joule heating in the high-latitude *F* region. *Deng and Ridley* [2007] used the Global Ionosphere Thermosphere Model (GITM) to perform global-scale numerical simulations of the Joule heating rate at high latitudes (60° MLAT and above) at 400 km altitude under moderate solar activity (*F*10.7 = 150) and $B_y = 0$. The postmidnight sector of their heating rate map [see *Deng and Ridley*, 2007, Figure 5] computed by GITM is similar to the postmidnight Joule heating region seen for solar maximum in the present study. The simulations of *Deng and Ridley* [2007] do not produce the observed postnoon Joule heating region, but this is likely due to differences between the neutral wind and ion convection data used as inputs to GITM (the empirical potential model of *Weimer* [1996] was used by *Deng and Ridley* [2007] as the high-latitude driver) and the neutral wind and ion velocity data used in the present study. For example, the large dusk rotation cell in the neutral winds of Figures 4 and 5 is almost nonexistent in Figure 4 of *Deng and Ridley* [2007].

Regions of heating are expected to be associated with increases in the scale height of thermospheric neutral density [e.g., *Carlson et al.*, 2012]. As the scale height of the neutral atmosphere increases, a density depletion in the heating region and a density enhancement above the heating region are expected to be observed. Furthermore, the dynamics involved with the increase in scale height are likely to drive vertical winds. Indeed, *Innis and Conde* [2001] observed enhanced vertical wind variability in the same location as the postmidnight heating region identified by this study.

The Swarm satellite mission, launched in November 2013, includes three satellites in orbit at two different altitudes. Each Swarm satellite is a next-generation version of CHAMP [*Friis-Christensen et al.*, 2008]. The Swarm satellites are capable of colocated in situ ion and neutral velocity measurements. Obtaining both measurements on a single spacecraft may eliminate uncertainty associated both with time variability on the order of minutes and with differing sampling altitudes that could not be addressed by the present study. The multi-satellite nature of the Swarm mission may also provide information about the relationship between short-, meso-, and global-scale heating. Furthermore, because Swarm is able to measure ion and electron temperatures, as well as ion and neutral wind velocities, it is possible to employ the technique of *St.-Maurice and Hanson* [1982] to obtain measurements of the thermospheric neutral temperature.

4. Conclusions

Combining ion and neutral wind data using the simplified ion energy equation of *St.-Maurice and Hanson* [1982], we have produced maps of high-latitude *F* region Joule heating in the Northern Hemisphere. These maps are split into solar maximum and solar minimum periods and further partitioned by IMF orientation. The main findings of this study are:

1. Two persistent heating regions are observed for both solar maximum and solar minimum conditions centered on 70° MLAT and 15 MLT (postnoon) and 70° MLAT and 2 MLT (postmidnight).
2. The postnoon region dominates during solar minimum and the postmidnight region dominates during solar maximum.
3. The extent and magnitude of the heating depend on IMF orientation, with $-B_z/+B_y$ conditions resulting in the largest extent and magnitude.

The results of this study are consistent with those of previous studies of high-latitude F region Joule heating; differences in the magnitude of the observed heating can be explained by the varying spatial and temporal averaging of data sets. Using GITM to model Joule heating in the polar thermosphere, *Deng and Ridley* [2007] were able to produce the postmidnight Joule heating region in Figure 6, but they did not find the postnoon heating region evident in the observations presented here.

The postmidnight heating region is located in a region that has been shown to have large variability in vertical neutral winds [*Innis and Conde*, 2001]. Joule heating induces an increase in the neutral density scale height and may drive vertical transport of neutral density, which may ultimately result in a neutral density depletion within the heating region and a neutral density enhancement above.

Coincident measurements of neutral wind, ion velocity, and plasma temperature on each of the Swarm satellites [*Friis-Christensen et al.*, 2008] will provide an opportunity to extend the techniques utilized in this paper to study F region Joule heating at finer temporal and spatial resolutions.

References

Baker, K. B., and S. Wing (1989), A new magnetic coordinate system for conjugate studies at high latitudes, *J. Geophys. Res.*, *94*(A7), 9139–9143, doi:10.1029/JA094iA07p09139.

Baron, M. J., and R. H. Wand (1983), *F* region ion temperature enhancements resulting from Joule heating, *J. Geophys. Res.*, *88*(A5), 4114–4118, doi:10.1029/JA088iA05p04114.

Carlson, H. C., T. Spain, A. Aruliah, Å. Skjæveland, and J. Moen (2012), First-principles physics of cusp/polar cap thermospheric disturbances, *Geophys. Res. Lett.*, *39*, L19103, doi:10.1029/2012GL053034.

Chisham, G., et al. (2007), A decade of the Super Dual Auroral Radar Network (SuperDARN): Scientific achievements, new techniques and future directions, *Surv. Geophys.*, *28*(1), 33–109, doi:10.1007/s10712-007-9017-8.

Cooper, S. L., M. Conde, and P. Dyson (2009), Numerical simulations of thermospheric dynamics: Divergence as a proxy for vertical winds, *Ann. Geophys.*, *27*(6), 2491–2502, doi:10.5194/angeo-27-2491-2009.

Cousins, E. D. P., and S. G. Shepherd (2010), A dynamical model of high-latitude convection derived from SuperDARN plasma drift measurements, *J. Geophys. Res.*, *115*, A12329, doi:10.1029/2010JA016017.

Cowley, S. W. H. (2000), Magnetosphere-ionosphere interactions: A tutorial review, in *Magnetospheric Current Systems, Geophys. Monogr. Ser.*, vol. 118, edited by S.-I. Ohtani et al., pp. 91–106, AGU, Washington, D. C., doi:10.1029/GM118p0091.

Cowley, S. W. H., and M. Lockwood (1992), Excitation and decay of solar wind–driven flows in the magnetosphere-ionosphere system, *Ann. Geophys.*, *10*(1-2), 103–115.

Davies, J. A., M. Lester, B. Jenkins, and R. J. Moffett (1995), Dayside ion frictional heating: EISCAT observations and comparison with model results, *J. Atmos. Terr. Phys.*, *57*(7), 775–793, doi:10.1016/0021-9169(94)00051-O.

Davies, J. A., M. Lester, and I. W. McCrea (1997), A statistical study of ion frictional heating observed by EISCAT, *Ann. Geophys.*, *15*(11), 1399–1411, doi:10.1007/s00585-997-1399-x.

Deng, Y., and A. J. Ridley (2007), Possible reasons for underestimating Joule heating in global models: *E* field variability, spatial resolution, and vertical velocity, *J. Geophys. Res.*, *112*, A09308, doi:10.1029/2006JA012006.

Doornbos, E., J. van den Ijssel, H. Lühr, M. Förster, and G. Koppenwallner (2010), Neutral density and crosswind determination from arbitrarily oriented multiaxis accelerometers on satellites, *J. Spacecr. Rock.*, *47*(4), 580–589, doi:10.2514/1.48114.

Dungey, J. W. (1961), Interplanetary magnetic field and the auroral zones, *Phys. Rev. Lett.*, *6*(2), 47–48, doi:10.1103/PhysRevLett.6.47.

Förster, M., S. Rentz, W. Köhler, H. Liu, and S. E. Haaland (2008), IMF dependence of high-latitude thermospheric wind pattern derived from CHAMP cross-track measurements, *Ann. Geophys.*, *26*(6), 1581–1595, doi:10.5194/angeo-26-1581-2008.

Friis-Christensen, E., H. Lühr, D. Knudsen, and R. Haagmans (2008), Swarm: An Earth observation mission investigating geospace, *Adv. Space Res.*, *41*(1), 210–216, doi:10.1016/j.asr.2006.10.008.

Fuller-Rowell, T. J., and D. Rees (1980), A three-dimensional time-dependent global model of the thermosphere, *J. Atmos. Sci.*, *37*(11), 2545–2567.

Goodwin, L., J.-P. St.-Maurice, P. Richards, M. Nicolls, and M. Hairston (2014), F region dusk ion temperature spikes at the equatorward edge of the high latitude convection pattern, *Geophys. Res. Lett.*, *41*, 300–307, doi:10.1002/2013GL058442.

Greenwald, R. A., et al. (1995), DARN/SuperDARN: A global view of the dynamics of high-latitude convection, *Space Sci. Rev.*, *71*(1–4), 761–796, doi:10.1007/BF00751350.

Gundlach, J. P., M. F. Larsen, and I. S. Mikkelsen (1988), A simple model describing the nonlinear dynamics of the dusk/dawn asymmetry in the high-latitude thermospheric flow, *Geophys. Res. Lett.*, *15*(4), 307–310, doi:10.1029/GL015i004p00307.

Hays, P. B., R. A. Jones, and M. H. Rees (1973), Auroral heating and the composition of the neutral atmosphere, *Planet. Space Sci.*, *21*(4), 559–573, doi:10.1016/0032-0633(73)90070-6.

Hays, P. B., J. W. Meriwether, and R. G. Roble (1979), Nighttime thermospheric winds at high latitudes, *J. Geophys. Res.*, *84*(A5), 1905–1913, doi:10.1029/JA084iA05p01905.

Heelis, R. A., and W. R. Coley (1988), Global and local Joule heating effects seen by DE 2, *J. Geophys. Res.*, *93*(A7), 7551–7557, doi:10.1029/JA093iA07p07551.

Heinselman, C. J., and M. J. Nicolls (2008), A Bayesian approach to electric field and *E*-region neutral wind estimation with the Poker Flat Advanced Modular Incoherent Scatter Radar, *Radio Sci.*, *43*, RS5013, doi:10.1029/2007RS003805.

Hunter, J. D. (2007), Matplotlib: A 2D graphics environment, *Comput. Sci. Eng.*, *9*(3), 90–95.

Innis, J. L., and M. Conde (2001), Thermospheric vertical wind activity maps derived from Dynamics Explorer-2 WATS observations, *Geophys. Res. Lett.*, *28*(20), 3847–3850, doi:10.1029/2001GL013704.

King, J. H., and N. E. Papitashvili (2005), Solar wind spatial scales in and comparisons of hourly wind and ACE plasma and magnetic field data, *J. Geophys. Res.*, *110*, A02104, doi:10.1029/2004JA010649.

Knipp, D., S. Eriksson, L. Kilcommons, G. Crowley, J. Lei, M. Hairston, and K. Drake (2011), Extreme poynting flux in the dayside thermosphere: Examples and statistics, *Geophys. Res. Lett.*, *38*, L16102, doi:10.1029/2011GL048302.

Liu, H., H. Lühr, S. Watanabe, W. Köhler, V. Henize, and P. Visser (2006), Zonal winds in the equatorial upper thermosphere: Decomposing the solar flux, geomagnetic activity, and seasonal dependencies, *J. Geophys. Res.*, *111*, A07307, doi:10.1029/2005JA011415.

Picone, J. M., A. E. Hedin, D. P. Drob, and A. C. Aikin (2002), NRLMSISE-00 empirical model of the atmosphere: Statistical comparisons and scientific issues, *J. Geophys. Res.*, *107*(A12), 1468, doi:10.1029/2002JA009430.

Reigber, C., H. Lühr, and P. Schwintzer (2002), CHAMP mission status, *Adv. Space Res.*, *30*(2), 129–134, doi:10.1016/S0273-1177(02)00276-4.

Ruohoniemi, J. M., and K. B. Baker (1998), Large-scale imaging of high-latitude convection with Super Dual Auroral Radar Network HF radar observations, *J. Geophys. Res.*, *103*(A9), 20,797–20,811, doi:10.1029/98JA01288.

Ruohoniemi, J. M., and R. A. Greenwald (2005), Dependencies of high-latitude plasma convection: Consideration of interplanetary magnetic field, seasonal, and universal time factors in statistical patterns, *J. Geophys. Res.*, *110*, A09204, doi:10.1029/2004JA010815.

St.-Maurice, J.-P., and W. B. Hanson (1982), Ion frictional heating at high latitudes and its possible use for an in situ determination of neutral thermospheric winds and temperatures, *J. Geophys. Res.*, *87*(A9), 7580–7602, doi:10.1029/JA087iA09p07580.

Strutz, T. (2010), *Data Fitting and Uncertainty: A Practical Introduction to Weighted Least Squares and Beyond*, Vieweg+Teubner Verlag, Wiesbaden, Germany.

Weimer, D. R. (1996), A flexible, IMF dependent model of high-latitude electric potentials having "Space Weather" applications, *Geophys. Res. Lett.*, *23*(18), 2549–2552, doi:10.1029/96GL02255.

Wilder, F. D., G. Crowley, S. Eriksson, P. T. Newell, and M. R. Hairston (2012), Ionospheric joule heating, fast flow channels, and magnetic field line topology for IMF by-dominant conditions: Observations and comparisons with predicted reconnection jet speeds, *J. Geophys. Res.*, *117*, A11311, doi:10.1029/2012JA017914.

Zhang, B., W. Lotko, M. Wiltberger, O. Brambles, and P. Damiano (2011), A statistical study of magnetosphere-ionosphere coupling in the Lyon-Fedder-Mobarry global MHD model, *J. Atmos. Sol. Terr. Phys.*, *73*(5–6), 686–702, doi:10.1016/j.jastp.2010.09.027.

Zhang, Q.-H., et al. (2013), Direct observations of the evolution of polar cap ionization patches, *Science*, *339*(6127), 1597–1600, doi:10.1126/science.1231487.